Proceedings of the ASME 2022
Internal Combustion Engine Division ICE Forward Conference
ICEF2022
October 16-19, 2022, Indianapolis, IN, USA

ICEF2022-90213

EVALUATION OF SPRAY AND COMBUSTION MODELS FOR SIMULATING DILUTE COMBUSTION IN A DIRECT-INJECTION SPARK-IGNITION ENGINE

Joohan Kim[1], Muhsin Ameen[1], Riccardo Scarcelli[1], Namho Kim[2], Eshan Singh[2], Magnus Sjöberg[2]

[1]Transportation and Power Systems Division, Argonne National Laboratory, Lemont, IL 60439
[2]Combustion Research Facility, Sandia National Laboratories, Livermore, CA 94551

ABSTRACT

Dilute combustion in spark-ignition engines has the potential to improve thermal efficiency by mitigating knock and by reducing throttling and wall heat losses. However, ignition and combustion processes can become unstable for dilute operation due to a lowered laminar flame speed, resulting in excessive cycle-to-cycle variability (CCV) of the combustion process. To compensate for the slower combustion in less reactive mixtures, a modified intake port geometry can be employed to generate a strong tumble flow in the cylinder and elevate turbulence levels around the spark plug, thereby promoting a faster transition to turbulent deflagration. Consequently, optimizing combustion chamber geometry and operating strategy is crucial to maximizing the benefits of using dilute combustion with enhanced in-cylinder turbulence across a wide range of operating conditions. Computational fluid dynamics (CFD) simulations can be utilized for virtual engine optimization tasks, but this would require the models to be truly predictive regarding the impact of changes to the engine design and operational parameters.

In this study, multi-cycle large-eddy simulations (LES) are performed for a direct-injection spark-ignition engine to investigate the model performance in predicting engine combustion characteristics with respect to changes in the intake configuration. A tumble plate that blocks the lower part of the intake port inlet is used to vary the tumble. A set of CFD models that have been recently developed are employed, which takes into account the drag of non-spherical droplets, flash-boiling behavior of liquid sprays, spray-wall interaction, surrogate formulation of a research-grade E10 gasoline, and fast chemical kinetic solvers. Simulation results are compared to experimental engine data in terms of cylinder pressure, apparent heat release rate, mass fraction burned timing, and flame images. It is found that LES employing the state-of-the-art CFD models are capable of properly predicting the spray processes and reproducing the measured mean cylinder pressure for the case with the tumble plate. On the other hand, the LES over-predicts the combustion rate during the early combustion stage and under-estimates the CCV, and these discrepancies become larger when the tumble plate is removed.

Keywords: Computational fluid dynamics simulation, large-eddy simulation, direct-injection spark-ignition engine, dilute combustion, cycle-to-cycle variability, tumble plate.

1. INTRODUCTION

Human economic activities heavily rely on transportation that connects people and distributes goods, while it mostly gains power from burning fossil fuels in internal combustion engines. According to the latest report published by U.S. Environmental Protection Agency (EPA) [1], the transportation sector accounted for the largest contribution of U.S. greenhouse gas (GHG) emissions amounting to 27% in 2020, of which passenger cars and light-duty trucks contributed 38% and 19%, respectively. To mitigate global warming and corresponding climate changes, federal regulatory agencies have continued to impose stringent regulations on GHG emissions from the transportation sector. U.S. EPA and National Highway Traffic Safety Administration have set tailpipe carbon dioxide (CO_2) emissions and Corporate Average Fuel Economy standards for passenger cars for the model year 2022 to be 180 g-CO_2/mile and 44.9 mpg, respectively, which will be further tightened to 168 g-CO_2/mile and 47.7 mpg by 2026 [2].

Dilute combustion is one of the key technologies that can improve the thermal efficiency of spark-ignition (SI) engines [3], which has recently been adopted by several automakers in the new engine development process [4]–[6]. In principle, either exhaust gas recirculation (EGR) or excess air can be used to dilute the mixture. However, the former is preferred today because the three-way catalytic converter in conventional SI engines favors a stoichiometric air-fuel mixture to achieve high conversion efficiency. Increasing dilution suppresses engine knock allowing operation with higher compression ratios and/or

© 2022 by ASME

maximum brake torque spark. Also, lowered combustion temperatures from dilute combustion help reducing the heat losses. Despite these advantages in thermal efficiency gain, combustion stability can be deteriorated due to the less reactive mixtures and low burning velocities, resulting in increased cycle-to-cycle variability (CCV) of the combustion process. As one of the measures to compensate for the reduced combustion rate, intake port and pent-roof geometries were modified to generate a stronger tumble flow while maintaining the volumetric efficiency with high flow coefficients [7]. Also, advanced ignition systems that allow greater coil energy and longer discharge duration were studied to ensure the stable ignition of diluted mixtures under enhanced turbulent conditions [8].

Computational fluid dynamics (CFD) simulations can assist the optimization during the engine development, which can save the time and cost if CFD models are accurate and predictive for a wide range of engine operating points and design changes. A number of models for each in-cylinder process (*e.g.*, turbulent flow, spray, ignition, combustion, pollutant formation, etc.) have been developed over the past few decades to improve simulation accuracy. The present study aims at investigating the integrated performance of the state-of-the-art models in predicting combustion characteristics of a direct-injection spark-ignition (DISI) engine with respect to a change in the intake configuration. Based on the large-eddy simulation (LES) framework, the current standard modeling approaches that are widely adopted in the engine modeling community are employed, including several sub-models and best practices that have recently been developed in the PACE (Partnership for Advanced Combustion Engine) program sponsored by the U.S. Department of Energy, Vehicle Technologies Office. The PACE models used in this study are for modeling drag of distorted droplets [9], [10], flash-boiling of liquid spray [11], spray-wall interaction [12], [13], multi-component surrogate fuel [14] and its detailed chemical mechanism [15] for a research-grade E10 gasoline, and using a fast chemical-kinetic solver [16], [17]. All the PACE models have been individually validated against relevant experimental data, but their integrated performance in engine simulations has not yet been extensively examined. In the current study, simulation results from the multi-cycle LES calculation are compared against experimental data obtained from an optically-accessible, single-cylinder research DISI engine.

In the following, the experimental setup of the optical DISI engine is provided in Section 2. This is followed by a description of the CFD modeling methodology in Section 3. Finally, in Section 4, simulation results with and without PACE models are presented first, and the predicted combustion characteristics such as cylinder pressure, apparent heat release rate (AHRR), mass fraction burned timings, and CCV are compared with the experimental data and analyzed for both intake configurations.

2. EXPERIMENTAL SETUP

The CFD results were compared with the experiments performed in a single-cylinder, four-valve, optically-accessible, direct-injection spark-ignition (DISI) research engine at Sandia National Laboratories. The key engine specifications and operating conditions are listed in Table 1, and the cross-section of the combustion chamber is shown in Fig. 1(a). Note that the crank angle degree (°CA) in the manuscript is referenced with respect to the firing top dead center. A centrally mounted 8-hole solenoid injector was installed close to the spark plug at a rotation to direct two spray plumes to straddle the ground electrode of the spark plug. Two optical apertures, one in the side of the pent-roof and the other one in the piston bowl, were used to image the ignition and combustion processes. In this study, a plate was installed to block 54% of the intake port inlet to generate a stronger tumble flow compared to the baseline configuration without the plate, as shown in Fig. 1(b).

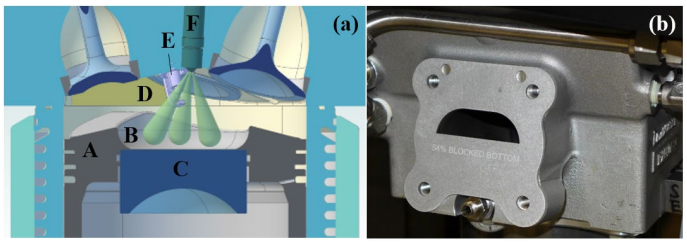

FIGURE 1: (a) Cross-sectional combustion chamber schematic at -35 °CA with (A) – piston; (B) – piston bowl; (C) piston bowl quartz window; (D) – pent roof quartz window; (E) – spark plug; (F) – fuel injector. (b) Intake port with a tumble plate.

TABLE 1: Engine specifications and operating conditions.

Engine specifications		
Displacement	L	0.552
Bore	mm	86.0
Stroke	mm	95.1
Connecting rod length	mm	166.7
Compression ratio	-	12:1
Engine operating conditions for Fire3-Skip9 operation		
Engine speed	rpm	1300
Coolant temperature	°C	~100
Average intake runner temperature	°C	70
Average intake runner pressure[1]	kPa	62
Spark timings for fired cycles	°CA	-30.9 (1st, 2nd) -24.9 (3rd)
Number of injections	-	3
Injection pressure	MPa	18
Injection duration per pulse	°CA	3.59
Actual start of injection (SoI_a) in a fired cycle	°CA	-307.4 (1st), -293.4 (2nd), -279.4 (3rd)
Fuel flow rate	mg/cycle	14.5
Air flow rate	mg/cycle	203.1

© 2022 by ASME

Diluent (N_2) flow rate	mg/cycle	93.0
Conventional equivalence ratio	-	1.0
Mass-based equivalence ratio	-	0.686

[1]No throttle was installed and the intake pressure was controlled by gas-metering nozzles, details provided in [21].

The engine was operated at 1300 rpm under fully warmed-up conditions. A coolant temperature of 100 °C was used. The average absolute pressure and temperature in the intake runner were maintained at 62 kPa and 70 °C, respectively. PACE-20 [14] (see Table 2 for fuel properties), a surrogate of a research-grade E10 gasoline, was injected early in the intake stroke using a triple injection strategy to form a well-mixed air-fuel mixture at the time of ignition. Considering the in-cylinder thermodynamic condition at the start of injections (SoIs) and the elevated fuel temperature (assumed to be similar to the coolant temperature), the liquid fuel spray would undergo flash boiling process [18]. Nitrogen (N_2) gas was used to dilute the intake charge air, targeting a mass-based equivalence ratio (see definition in Eq. 1) of 0.686, which is equivalent of rerouting 30% of the exhaust flow back into the intake (apart from the fact that real EGR would contain CO_2, H_2O, and minor species). Note that the conventional equivalence ratio (ϕ), which only considers air and fuel, was kept at unity to maintain stoichiometric combustion.

$$\phi_m = \frac{\left({}^{Fuel}/_{Air+Diluent}\right)_{actual}}{\left({}^{Fuel}/_{Air}\right)_{stoichiometric}}, \quad (1)$$

TABLE 2: Liquid surrogate fuel (PACE-20) properties.

Components	(%, liquid volume fraction)	ethanol (9.55) n-pentane (13.95) cyclopentane (10.50) 1-hexene (5.41) n-heptane (11.53) toluene (9.19) iso-octane (25.05) 1,2,4-trimethylbenzene (11.87) tetralin (2.95)
Density	g/mL	0.74
Research/Motor Octane Number	-	92.1 / 84.5
H:C ratio	-	1.97
Distillation temp., T10 / T50 / T90	°C	57.9 / 89.9 / 166.0

The engine was operated in a repeating Fire3-Skip9 sequence to reduce the thermal loading on the quartz windows. The images were recorded only for the third fired cycle where the thermal boundary condition is hotter and closer to that of the all-metal continuously fired operation. Furthermore, the residual gas composition of third cycle is more representative of the all-metal continuously fired operation than the first two cycles since the residuals of the first cycle contain only air. It should be noted that the first two fired cycles used more advanced spark timing (ST, -30.9 °CA) than the third cycle (-24.9 °CA) to compensate for the low thermal state of the engine, which would otherwise lead to unstable combustion and makes it difficult to establish thermal boundary condition and residual gas compositions needed for the third cycle. The elevated intake air temperature (70 °C) also helped to stabilize the combustion process under the skip-fired operation with short overall runtime.

Details on the dual camera setup used for imaging combustion natural luminosity from chemiluminescence and hot soot can be found in [19]. A Phantom v710 monochrome camera was used for imaging via the optical aperture from the side of the combustion chamber. A Phantom v611 RGB color camera was used to acquire bottom-view images via the 45° Bowditch mirror and piston window. Both cameras were operated synchronously, recording 150 images per cycle using the identical frame rate (26 kHz) and exposure time (35 μs). For v710, the f-stop of f/4 was used with a 50 mm lens to collect sufficient amount of light. For v611, the f-stop of f/2.8 was used with a 180 mm lens to maximize the light collection while maintaining reasonably sharp images. A total of 150 images per cycle were recorded starting 0.3 °CA before the spark timing at an interval of 0.3 °CA, effectively capturing the combustion processes from the start to the end.

Pressures for the combustion chamber, intake runner, and exhaust tank were measured with 0.1 °CA resolution. The measured pressure data from only the third fired cycle was used to compute net indicated mean effective pressure (nIMEP), coefficient of variation of nIMEP (COV_{nIMEP}), and AHRR. The AHRR was computed using a constant ratio of specific heats (γ=1.33) following Heywood [20]. For computing combustion-phasing metrics like the 50% burn point (CA50), the AHRR was integrated over the crank-angle range for which AHRR is positive, after the spark discharge. Addition of diluents can affect γ, and the resultant burn point calculations. However, in a previous study, it was found that the change in γ due to diluent is relatively small, contributing with less than ±0.1 °CA to the uncertainty of CA50 [21].

3. Numerical Setup

Simulations are performed using CONVERGE CFD v3.0 [22], a commercial CFD solver that automates the mesh generation process and allows using simple orthogonal grids, fixed embedding, and adaptive mesh refinement (AMR). A collocated finite volume approach is used to compute the conservation equations of mass, momentum, energy, and species transport. A modified Pressure Implicit with Splitting of Operator (PISO) method is employed for an iterative algorithm, and an additional Jacobi iteration for all quantities is performed to enforce strict conservation. A second-order central-differencing scheme is used for the spatial discretization, and a first-order implicit Euler scheme is used for the time advancement.

Figure 2 shows the computational domain of the research engine and the grid configuration for the combustion chamber.

© 2022 by ASME

Also, the coordinate system for the side and bottom views are also noted as a reference for the discussion in later sections. The base grid size is 4 mm, and the grid is further refined using four fixed embeddings: 1 mm for the engine cylinder region, 0.5 mm for the wall boundaries, 0.25 mm for the spray region, and 0.125 mm for the spark plug region. In addition, a sub-grid scale-based AMR is employed to automatically refine the base grid down to 0.5 mm by monitoring the sub-grid fields of velocity, temperature, and progress variable. The last two variables are only activated during the combustion process to resolve the turbulent flame propagation better. The order of numerical schemes in time and space discretization and the grid size are regarded as an engineering LES rather than the conventional LES that requires higher-order schemes and smaller grid sizes [23]. Nonetheless, the grid configuration used in this study has been proven to be valid for reproducing experimental cyclic variability in-cylinder pressures [24].

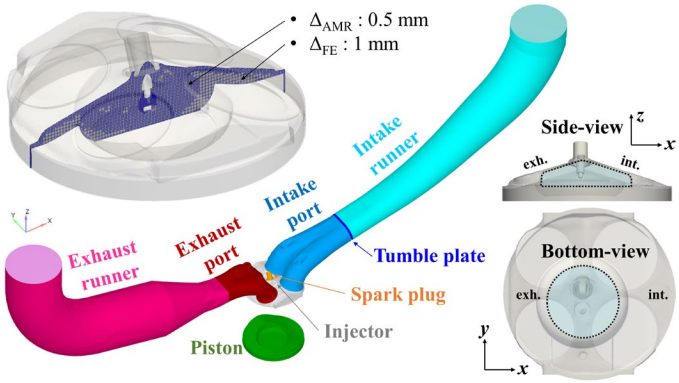

FIGURE 2: Computational domain and grid configuration.

The crank-angle resolved pressure boundary conditions are imposed at the inlet and outlet of the intake and exhaust runners while applying constant temperature boundary conditions. Based on the measured temperatures of the fire-deck and coolant, the wall temperature of the combustion chamber is set at 105 °C. The measured rate of injection profile for an iso-octane fuel is used for the fuel-flow rate with a density correction.

In this study, a set of the state-of-the-art CFD models that have been developed in the PACE consortium are employed, including the Corrected Distortion model [9], [10], the best practices for flash-boiling spray with the KH-RT (Kelvin-Helmholtz Rayleigh-Taylor) model [11], the spray-wall interaction model [12], the detailed chemical mechanism for the PACE-20 surrogate fuel [14], and the Zero-order Reaction Kinetic (Zero-RK) solver [16], [17]. Since the selected engine operating point is under flash-boiling conditions and there is potential for spray impingements on the piston and valves, the PACE models are expected to improve simulation accuracy for the spray process. Before presenting an overview of the PACE models, the other CFD models for simulating the in-cylinder physics (flow, spray, ignition, and combustion) are briefly discussed. Detailed information on each CFD model can be found in the corresponding literature.

The turbulent flow is modeled using the Dynamic Structure model [25] based on the large-eddy simulation (LES) framework. For the liquid fuel injection, the primary and secondary breakup processes are modeled using the Blob injection model [26] and the KH-RT model [27]. The effect of the turbulent flow on the liquid drops is taken into account by the O'Rourke turbulent dispersion model [28]. For the spark ignition and turbulent combustion processes, an energy deposition approach and the G-equation model [29] are employed. At the ignition timing, spark energy that is assumed to be an L-shape power profile (breakdown: 25 mJ for 0.5 °CA, glow discharge: 75 mJ for 15.2 °CA) is deposited into a spherical control volume (radius of 0.4 mm) located at the electrode gap center. Then, an iso-surface of $\tilde{G} = \tilde{G}_0(\vec{x}, t)$ is initialized where the gas temperature exceeds 3,000 K by the spark energy deposition, and the G-equation model starts to track the propagating flame. The species composition behind the flame front is assumed to be in the chemical equilibrium, and no chemical reaction mechanism is explicitly solved in the computational domain for the sake of computational efficiency. Also, emissions predictions against the experimental data obtained from the skip-fired operation are not relevant, so no emissions models are used in the simulation and the chemical equilibrium assumption is considered valid. On the other hand, the investigated engine operating conditions did not trigger engine knock, so no auto-ignition chemistry is solved in the unburned region.

3.1 Corrected Distortion Model

Dahms et al. [9] developed the Corrected Distortion model that is accounting for the effects of non-spherical drops on the drop drag and evaporation formulation. Recently, Nguyen et al. [10] validated the model with high-quality experimental measurements under engine relevant conditions. As a brief summary of the modeling methodology, firstly, the drag coefficient (C_D), Sherwood (Sh), and Nusselt (Nu) numbers for viscous spherical drops are computed using correlations proposed by Feng and Michaelides [30], [31]. Then, a regression model for viscous distorted drops [32] is applied to the above three variables with consideration of the increased surface area of distorted drops. The resultant C_D, Sh, Nu are updated in the equation of drop motion, the rate of change of drop radius by evaporation, and the rate of heat conduction to the drop surface, respectively. Without activating the Corrected Distortion model, the default modeling approaches for C_D, Sh, Nu follow the Taylor Analogy Breakup model [33], Frossling correlation [28], and Ranz-Marshall correlation [34].

3.2 Best Practices for Flash-Boiling Spray with KH-RT Model

When a liquid spray undergoes flash-boiling, this can cause spray-plume merging and spray collapse for a multi-hole injector [35]. For modeling a flash-boiling spray, several researchers have developed CFD models for either phase

© 2022 by ASME

change [36], [37] by bubble cavitation, heat transfer at the liquid-gas interface, and superheating of liquid fuel, or atomization [38] by aerodynamic force and bubble growth. Although the KH-RT model only computes mechanical atomization by monitoring instabilities induced by velocity shear or drop acceleration, Guo et al. [11] demonstrated that calibrating the KH-RT's model constants could be effective to mimic the thermal atomization by flash-boiling under various fuel temperatures and engine speeds. To this end, for the given thermal and flow conditions (*i.e.*, fuel and coolant temperature and engine speed) used in this study, the time constant (C_I) and the size constant (C_{RT}) the RT breakup regime are modified to 0.1 and 0.25 (cf. default values are 1.0 and 0.5) respectively. In addition, the spray cone angle is adjusted to 35° to better simulate the spray collapse.

3.3 Spray-Wall Interaction Model

Torelli et al. [12] developed a spray-wall interaction model with a novel method for impingement frequency calculation to improve drop splash predictions. As a brief description of the modeling methodology, firstly, they identified that the droplet spacing of a spherical cloud impinging on a wall was smaller than the maximum spreading radius on the wall of a train of droplets. Then, they modified the traditional zero-droplet-spacing assumption for the impingement frequency calculation to consider droplet inter-collision in three-dimensional space. Lastly, a wall roughness model was implemented to reproduce realistic recirculation and shape of the rebounded spray leading edge. Recently, the developed model has been further applied to DISI engine simulations and well-matched fuel film area deposited on the piston wall against the experimental data [13].

3.4 Laminar Flame Speed Tabulation with Detailed PACE-20 Mechanism and Zero-RK Solver

In the G-equation model, a flame-speed correlation proposed by Pitsch [39] is used to predict turbulent flame speed (s_t) of the propagating flame front, which is defined as

$$s_t = s_l\left(1 - \frac{b_3^2 s_l}{2b_1 u'}\frac{\mu_t}{\mu} + \sqrt{\left(\frac{b_3^2 s_l}{2b_1 u'}\frac{\mu_t}{\mu}\right)^2 + b_3^2\frac{\mu_t}{\mu}}\right), \qquad (2)$$

where s_l is the laminar flame speed, u' is the sub-grid scale velocity, μ_t is the turbulent viscosity, μ is the molecular viscosity, and b_1 and b_3 are the model constants. In this study, a four-dimensional flame database is referred to during the engine simulation, which is pre-tabulated with the Zero-RK solver [16], [17] that computes the one-dimensional premixed flames using the PACE-20 detailed chemical mechanism (4212 species, 19134 reactions) developed by Wagnon and his co-workers [15]. The flame table covers the temperature, pressure, equivalence ratio, and diluent mass fraction for 600-900 K by 50 K step, 5-45 bar by 5 bar step, 0.6-1.4 by 0.1 step, and 0-35% by 5% step, respectively.

4. RESULTS AND DISCUSSION

4.1 Comparison of PACE Models and CONVERGE Standard Models

Simulations are carried out to investigate the impact of the PACE models on liquid spray behavior, fuel-film wetting, and air-fuel mixture preparation. Table 3 summarizes the references of PACE models and CONVERGE standard models for each in-cylinder physics, and Table 4 lists four model combinations used for the comparison. All the simulations start at the SoI of the first injection with the same field variables ($\vec{u}, T, P, Y_i, k$) to keep the initial condition identical.

TABLE 3: Numerical models for in-cylinder physics: PACE models (left) and CONVERGE standard models (right).

Physics		*PACE*	*CONVERGE*
Droplet distortion (DD)	C_D	Nguyen et al. [10]	Taylor Analogy Breakup [33]
	Nu		Frossling correlation [28]
	Sh		Ranz-Marshall correlation [34]
Flash-boiling (FB)	Phase change	Adachi et al. [37]	Adachi et al. [37]
	Atomization	Guo et al. [11]	N/A
Spray-wall interaction (SWI)		Torelli et al. [12]	O'Rourke and Amsden [40]

TABLE 4: Model combinations for comparison.

Name	*Combination*
PACE-All	PACE models for all physics (DD, FB, SWI)
Standard-DD	Standard model for DD; PACE models for FB, SWI
Standard-FB	Standard model for FB; PACE models for DD, SWI
Standard-SWI	Standard model for SWI; PACE models for DD, FB

The model combination of PACE-All has remarkable impacts on the liquid fuel spray behavior as shown in Fig. 3, where projected liquid volume (PLV) is used to quantitatively visualize the cross-stream liquid volume fraction. The Standard-SWI result is not presented because it shows the same spray dynamics as the PACE-All before impinging on the piston. Overall, the PACE-All shows a wider spray plume width at the downstream location (z < 10 mm) and less deflected spray plumes, compared to the Standard-DD. During the third injection, the spray plumes on the right-hand side (x > 0 mm, intake side) are perturbed by the intake charge motion as the intake mass flow rate increases (maximum intake valve lift occurs at -251 °CA), leading to the asymmetric spray structure. Nonetheless, the PACE-All shows a less altered spray than the Standard-DD. Dahms et al. [9] showed that the Corrected

© 2022 by ASME

Distortion model computes a lower drag coefficient than the Taylor Analogy Breakup approach [33] at a given droplet's distortion factor. Hence, the injection velocity of the liquid droplets would be less affected by the ambient gas, leading to a less deflected spray plume downstream as observed in the PLV contour. On the other hand, the PACE-All can capture the collapsed spray structure by the flash-boiling, whereas in the Standard-FB each spray plume maintains the initial injection direction and plume cone angle. Due to un-collapsed spray structure, some degree of spray-valve interaction is also observed as a high PLV on the intake side ($0 < x < 5$ mm, $5 < z < 20$ mm).

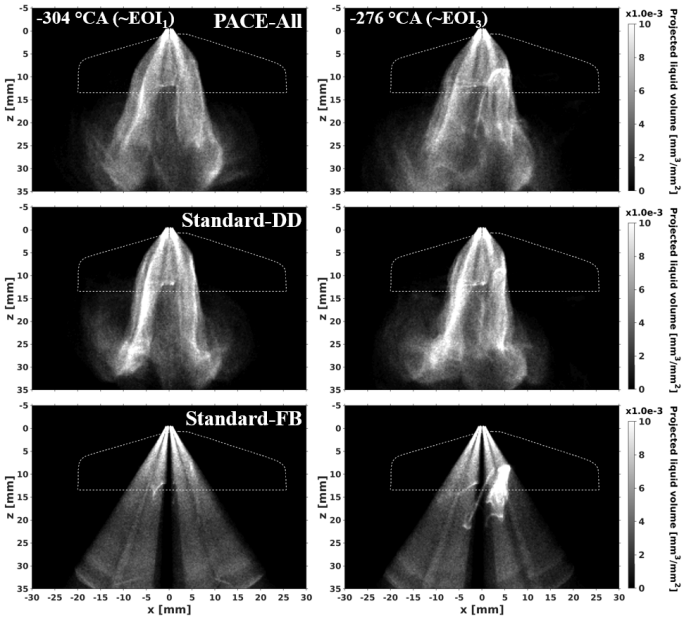

FIGURE 3: Comparison of liquid spray structure using the projected liquid volume for different model combinations: PACE-All, Standard-DD, and Standard-FB. Timings close to the end of the first (left) and the third (right) injection are selected.

Different spray dynamics result in different spray-wall interactions, as revealed in the fuel-film wetting contour (Fig. 4). Compared to the Standard-DD, the PACE-All combination predicts a larger area of fuel-film wetting after the first injection event, attributed to the higher velocities of the liquid droplets colliding with the piston, which are due to smaller drag coefficients. Also, as the fuel injection continues, the fuel-film is more uniformly spread in the piston bowl than the Standard-DD. Since the Standard-DD predicts a more deflected spray structure, the fuel-film is mostly concentrated in the center of the piston bowl, and a thick fuel-film spot lasts until the bottom dead center (BDC). The Standard-FB leaves a distinct spray footprint on the piston with clear boundary of each fuel-film spot that does not overlap with others. This is because no spray collapse is reproduced in the Standard-FB model combination. Also, it can be seen that one of the fuel-film spots on the intake side is cut in half, which corresponds to the spray-valve interaction. For the Standard-SWI, it is interesting that the fuel-film mass deposited from the first injection is smaller than the PACE-All, even though both spray dynamics before the impingement are identical. Also, the fuel-film mass left at the BDC is different, despite the similar fuel-film distribution during the second and third injection events. It is found that, in the Standard-SWI result, the maximum fuel-film height at the end of the second injection is 1.1 μm, which is 20% thicker than the PACE-All.

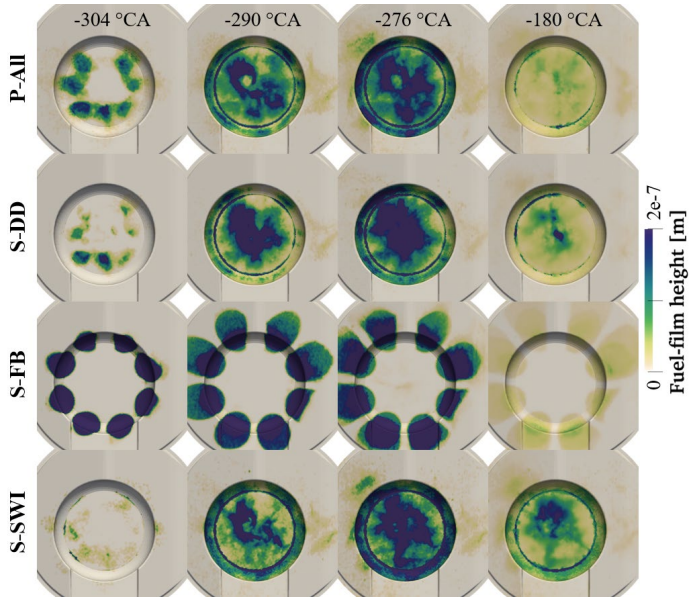

FIGURE 4: Comparison of fuel-film height and distribution for different model combinations: PACE-All, Standard-DD, Standard-FB, and Standard-SWI. Timings of the end of the first, second, and third injection and BDC are selected.

Although the spray structure and fuel-film distribution appear different for the selected model combinations, the temporal evolution of the in-cylinder mixture ϕ and the total fuel-film mass deposited on the piston are similar to each other except for the Standard-FB, as shown in Fig. 5. For example, during the injection, the Standard-DD shows slightly faster evaporation that leads to greater ϕ, as well as a slightly larger fuel-film mass. Then, the differences become barely discernable as the air-fuel mixing and fuel-film evaporation continue. Nonetheless, both the statistical and spatial distribution of mixture ϕ are different. The bar graph of mixture ϕ-distribution in Fig. 5(c) shows that, at the spark timing, the PACE-All predicts the highest mass fraction of near stoichiometric mixture, whereas the Standard-SWI results in the largest mixture stratification. To take a closer look at the in-cylinder mixture field, each spatial ϕ-distribution is distinct and implies that air-fuel mixing process during the intake and compression strokes is highly turbulent.

© 2022 by ASME

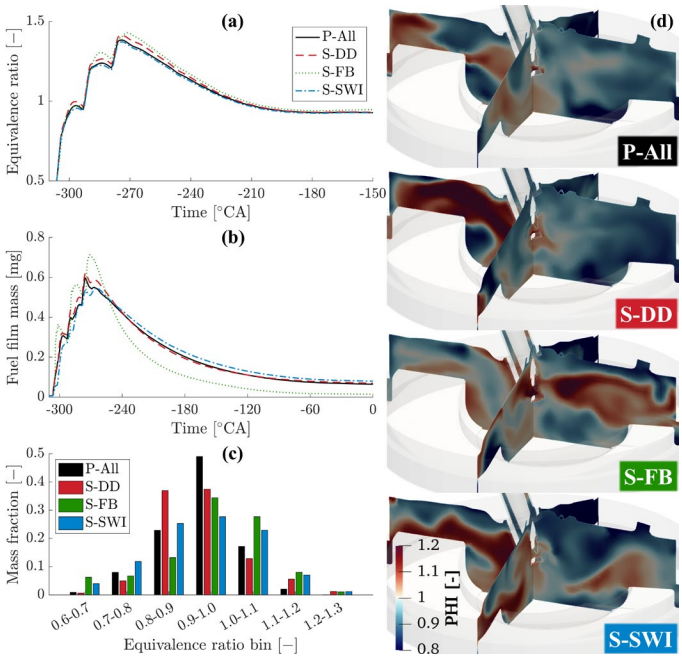

FIGURE 5: (a) Time history of gas-phase in-cylinder mixture equivalence ratio; (b) Time history of liquid fuel-film mass deposited on combustion chamber walls; (c) Mixture equivalence ratio distribution at spark timing; (d) Spatial mixture equivalence ratio distribution for four different model combinations: PACE-All, Standard-DD, Standard-FB, and Standard-SWI.

4.2 Comparison of Experimental Data and LES Result

Using the PACE-All combination, LES is performed for the selected engine operating condition with tumble plate installed in the intake port. In the LES calculation, instead of replicating the Fire3-Skip9 engine operation, a consecutive fired-cycle run is performed for 26 LES cycles. This assumes that transient change in the wall thermal conditions during the motored cycles is negligible, and the boundary condition of temperature and residual compositions for the third fired-cycle is replicable throughout the engine test. Note that the first LES cycle is discarded from the results presented in the paper. Accordingly, a total of 25 consecutive-fired LES results are compared against 50 skip-fired cycles from the experimental data. The maximum cell count is 3 million with the numerical setup, and the turnaround simulation time is 20 hours per cycle using 144 processors (Intel Xeon E5-2695V4) on the Bebop cluster at Argonne Laboratory Computing Resource Center.

The LES result is compared with the experimental data for the cylinder pressure, AHRR, and the combustion duration in Fig. 6. From the combustion metrics listed in Table 5, it can be seen that the LES underestimates the combustion duration of the early stage from ST to CA10, then it overpredicts the duration for the remainder combustion process. Considering the mean AHRR, the LES result shows an earlier rise in heat release rate compared to the experiments, as shown in terms of an earlier HRR1 (time of AHRR exceeding 1 J/°CA). This leads to an earlier CA10 in the LES. Thereafter, the experimental data shows a higher heat release rates and reaches CA50 faster than the LES. An earlier CA10 and later CA50 in the simulation results in an extended CA10-50 duration and a high prediction error of 37.9%. The retarded CA50 timing also affects the magnitude of the peak cylinder pressure (PCP), and hence the mean PCP is slightly underpredicted in the LES.

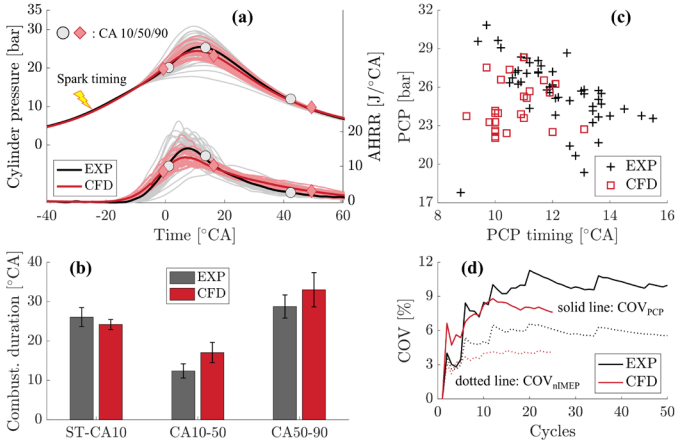

FIGURE 6: Comparison of experimental data and LES result for (a) cylinder pressure and AHRR; (b) combustion duration; (c) correlation between PCP timing and magnitude; (d) convergence histories for COV_{PCP} and COV_{nIMEP}.

TABLE 5: Key combustion metrics.

		EXP	LES	Error [%]
Combustion duration [°CA]	ST-CA10	26.1	24.2	-7.3
	CA10-50	12.4	17.1	37.9
	CA50-90	28.8	33.0	14.6
nIMEP [bar]		3.55	3.66	3.1
COV_{nIMEP} [%]		5.6	4.1	-1.5 (abs.)
PCP [bar]		25.6	24.6	-3.9
COV_{PCP} [%]		9.9	7.6	-2.3 (abs.)

Using the combustion images acquired in the experiment, the discrepancy of the early combustion stage (ST-CA10) is further investigated. Figure 7 presents experimental images and simulated flame contours from the side-view for a cycle with combustion metrics (cylinder pressure trace, peak pressure and combustion phasing) close to the mean cycle. As discussed above, the experimental image captures the natural luminosity so that both the spark channel and flame kernel are recorded in a single image with different light intensities of the grayscale. It is shown that the spark channel emits luminous light (saturated, white color) and is highly elongated in the first few crank angles, depositing the spark energy to the air-fuel mixture near the spark plug. The burned gas with temperatures relatively lower than the spark channel can be seen in the image of -22 °CA, which is visualized with a less intense luminosity (gray color). Then, the volume of the burned gas becomes larger as the flame kernel grows, and it can be distinguished from the

© 2022 by ASME

spark channel, as shown in the image of -18 °CA. In contrast to the experimental observations, the simulated flame contour shows an immediate flame kernel inception right after the spark timing, of which enclosing volume is much larger than the electrodes gap region. Although the flame front is initialized by the G-equation model when the cell temperature exceeds 3,000 K, the iso-surface of G=0 does not coincide with the iso-surface of T=3,000 K because of numerical treatments [41]. Once the iso-surface of G=0 is initialized, the model tracks the flame front using the turbulent flame speed correlation, which overpredicts the burn rate for the early flame kernel growth stage. Therefore, such fast flame kernel inception and a large burn rate explains why the CA10 phasing is advanced compared to the experimental data. Also, the ignition modeling approach used here is not capable of simulating spark channel behaviors (elongation, short-circuit, blow-out/restrike), which could deteriorate the simulation accuracy. Even if the spark channel elongation is captured by a sub-model, its effect on the flame kernel growth would not be impactful due to the over-estimation of the initial flame kernel size that could fully enclose the spark channel motion. Thus, advanced ignition models for spark channel behaviors, realistic energy deposition, and flame kernel growth [42] need to be considered in a future study.

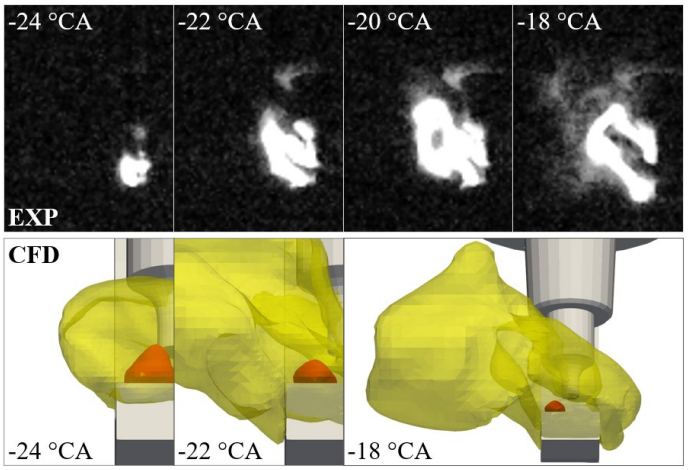

FIGURE 7: Comparison of experimental images and simulation results for early flame kernel growth from side-view. Two iso-surfaces for G=0 (yellow) and T=3,000 K (red) are selected to indicate boundaries of burned gas and spark energy depositing volume.

Figure 6(d) shows that the evolution of COV_{nIMEP} and COV_{PCP} as a function of the number of cycles used for statistics. It can be seen that around 15 cycles are needed for a proper convergence. Both COV_{nIMEP} and COV_{PCP} in the LES result are under-predicted by 1.5% and 2.3% (absolute percentages) respectively. On the other hand, one can notice that, in the measured cylinder pressure traces, there are two cycles showing very low PCP and retarded combustion phasing, and their nIMEP are ~20% off from the mean value. Such a slow burn is not captured in the simulation. Except for the two extreme cycles, the CCV span prediction agrees with the experimental data, where the differences in the LES and experimental COV_{nIMEP} and COV_{PCP} become 0.3% and 0.7% (absolute percentages) respectively.

In SI combustion process, a more advanced combustion phasing would lead to a higher PCP. The LES result is used to analyze the CCV, which is shown in Fig. 8. From Fig. 8(a), it is obvious that the PCP is correlated well with the CA50 timing, showing a high R^2 of 0.959. To better understand the reasons for CCV, PCP is also plotted against CA10, CA5, and the HRR1. Both CA10 (R^2=0.766) and CA5 (R^2=0.712) are well correlated to the PCP, but the correlation is rather poor for HRR1 (R^2=0.493).

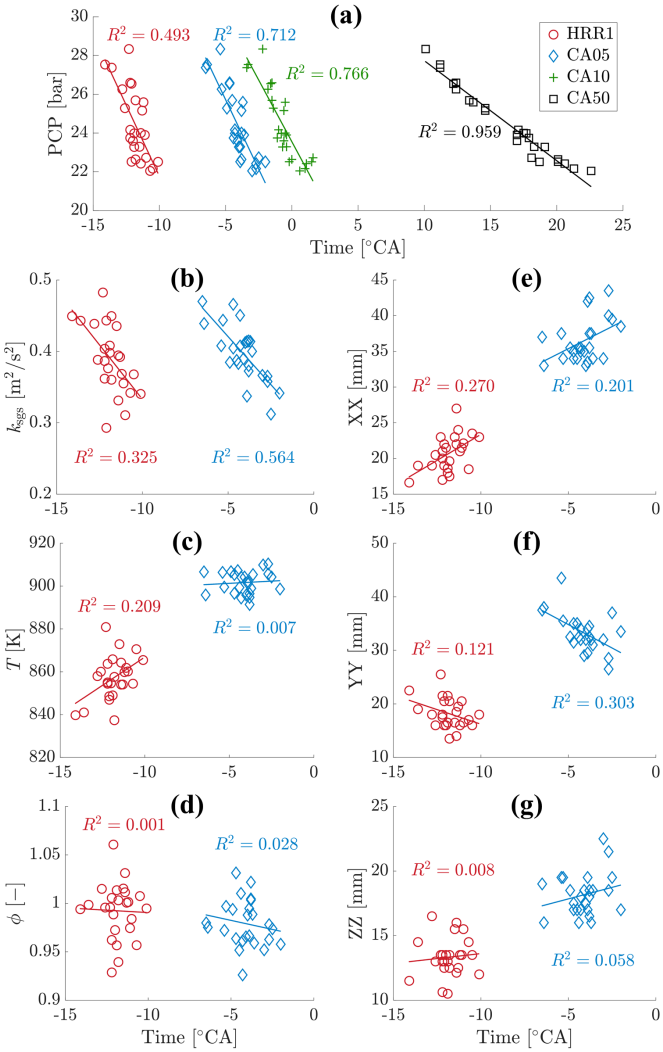

FIGURE 8: CCV analysis using LES result. Timings of HRR1 (red circle), CA5 (blue diamond), CA10 (green plus), and CA50 (black square) are correlated with (a) peak cylinder pressure; (b) sub-grid scale turbulent kinetic energy; (c) temperature; (d) equivalence ratio; (e) span of burned volume in *x*-direction; (f) that in *y*-direction; (g) that in *z*-direction.

Analyzing the flow and mixture conditions at early timings (HRR1 and CA5) has the potential to reveal which properties

© 2022 by ASME

have the most impact on the combustion rate. Furthermore, the variation of properties would be linked to the CCV of the combustion process, so the cause of CCV can be analyzed. Thus, three variables, sub-grid scale turbulent kinetic energy (k_{sgs}), temperature, and mixture equivalence ratio, that are responsible for calculating the turbulent flame speed in Eq. (2), are mass-averaged in a zone that is defined as -1e-3 < G < 0, namely the unburned region ahead of the flame front (G=0). This post-processing is performed for HRR1 and CA5 timings of all LES cycles, as shown in Fig. 8(b)-(d).

Among the examined properties, it is clear that the k_{sgs} shows the highest correlation with the combustion phasing of HRR1 and CA5. The slope of the trend line implies that a greater k_{sgs} typically results in an earlier combustion phasing and a higher PCP. The correlation becomes more significant at CA5 (R^2=0.564). On the other hand, unburned temperature and mixture equivalence ratio are almost not correlated with the two combustion phasing. Although the unburned temperatures at HRR1 show a weak correlation (R^2=0.209), it does not align with the common expectation that a higher unburned temperature would lead an earlier combustion phasing. Instead, the temperature versus time seems to reflect the effect of piston compression on the gas temperature. Unlike the variation in k_{sgs}, the fluctuation in the temperature and ϕ are small, and their impacts on the laminar flame speed would be negligible. Therefore, turbulent flow properties have the most impact on the combustion rate, and its variability largely affects the CCV of the combustion process.

The spans of the burned volume (G > 0) are computed for x-, y-, and z-direction (*e.g.*, XX means the length of burned volume in x-direction) and plotted in Fig. 8(e)-(g). It can be seen that the flame growth in z-direction is least correlated with the two combustion phasing metrics, while its growths in x- and y-directions have relatively significant correlations. Considering only correlation with the CA5 result, the shape of burned volume appears to be more elongated in the y-direction if the combustion phasing is advanced, while it is more elongated along the x-direction if the combustion phasing is retarded.

The simulation result is further compared with the optical images taken from the bottom-view, as shown in Fig. 9. Two LES cycles with the highest and the lowest PCP (hereafter high- and low-cycle) are compared to the experimental data that have similar PCP magnitudes. With the same angle of view, a volume-rendering of temperature is used for visualizing the LES result, while the natural luminosity of the flame is shown for the experimental data. Note that, in the simulation result, the spark plug is not shown and the bottom-view is not confined by the area of the quartz window. Figure 9 reveals that the LES result is able to reproduce the measured flame shape features in both datasets: almost uniform propagation of the flame in the high-cycle (see image at time of -12 °CA), whereas asymmetric combustion in the low-cycle (time of -9 °CA). It is interesting to see that, in the low-cycle, the flame propagation in the y-direction is suppressed and takes place much later (not shown here). This is consistent with the observations for CA5 in Fig. 8(f). By analyzing the flow and mixture field of the low-cycle, as shown in Fig. 10, it is revealed that the flame mainly follows the bulk flow motion that has already been established earlier (see image at time of -20 °CA), where the in-cylinder charge flows towards the exhaust side (left-hand side of the image) with velocities beyond 10 m/s. This strong flow motion is attributed to the tumble plate installed in the intake port. On the other hand, the upper part of the flame also encounters lean air-fuel mixtures that lower the laminar flame speed, mitigating the flame propagation upward (positive y-direction).

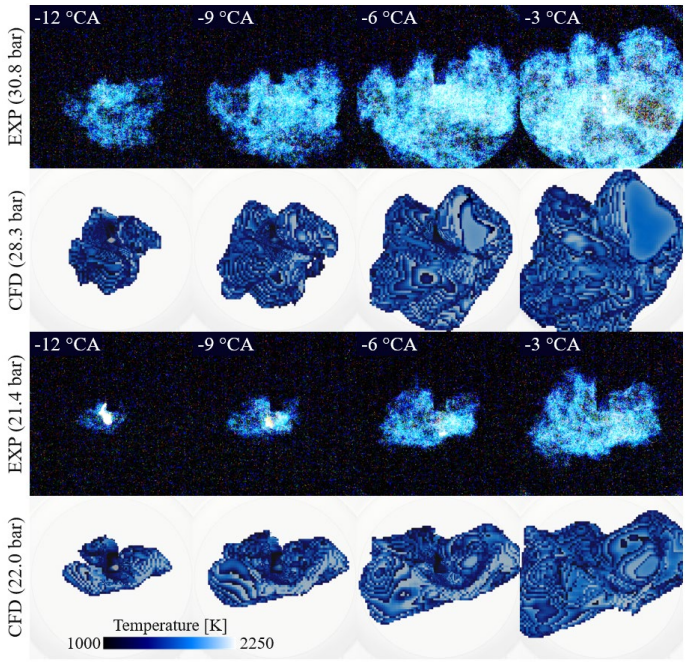

FIGURE 9: Comparison of measured combustion natural luminosity and simulated burned volume for the high- and low-cycles from bottom-view. A volume-rendering of temperature is used for LES result visualization.

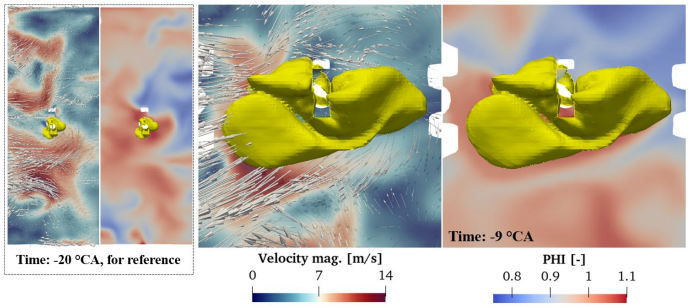

FIGURE 10: Low-cycle at -9 °CA: bottom-view of flow and mixture fields using velocity contour (left) and equivalence ratio contour (right). An iso-surface of G=0 colored in yellow represents the flame front.

Figure 11 shows the temporal evolution of projected flame area obtained from the bottom view through the quartz window in the piston (diameter: 37.4 mm). Note that the same confined

© 2022 by ASME

view window is applied to the LES results. As discussed above, the LES over-predicts the burn rate in the early combustion stage, and the size of the flame in terms of the projected flame area is larger than that observed in the experimental data.

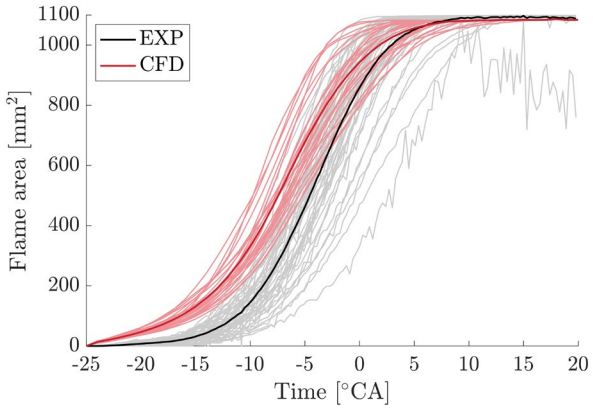

FIGURE 11: Comparison of measured and simulated projected flame area from the bottom.

4.3 Prediction of Intake Design Change

LES calculation is performed for the intake port geometry without the tumble plate (TP), and 25 LES cycles are analyzed in this section. Firstly, the effects of the tumble plate on flow properties and combustion metrics are discussed. Figure 12(a) presents the tumble ratio with respect to the y-axis for the two intake port configurations. It is shown that the tumble ratio is reduced by almost two-thirds by removing the tumble plate, including the peak tumble ratio and the value at the spark timing. The mass-averaged flow velocities around the spark plug are also compared and plotted in Fig. 12(b). In contrast to the with-TP case, the mean flow velocities indicate that the mixture near the electrodes flows toward the exhaust side (negative *x*-direction) and downward (negative *z*-direction). Meanwhile, there are substantial fluctuations in the flow velocities so that the flow directions may change cycle-to-cycle. Table 6 lists the measured combustion metrics for the two cases. As the tumble intensity is reduced in the without-TP case, the combustion durations for both early stage and main combustion become longer so that the CA50 timing is also significantly retarded. Consequently, the COV_{nIMEP} is doubled while the nIMEP is lowered more than 15% compared to the with-TP case.

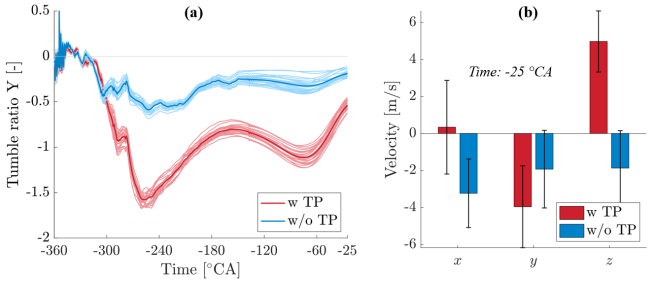

FIGURE 12: Comparison of with TP and without TP cases for (a) tumble ratio Y; (b) velocity around the spark plug at -25 °CA. Mass-average is performed for flow velocities in a spherical control volume (radius: 2 mm) located at the electrode center.

TABLE 6: Comparison of measured combustion metrics.

EXP data	w/ TP	w/o TP
ST-CA10 [°CA]	26.1	32.2
CA10-90 [°CA]	41.2	58.2
nIMEP [bar]	3.55	2.97
COV_{nIMEP} [%]	5.6	11.2

It is worth examining whether the LES can capture the measured trend according to the change of the intake configuration. The LES result for the combustion process is summarized in Fig. 13 and Table 7. The predicted mean cylinder pressure agrees quite well with the experimental data, but the span of pressure traces in the LES result is much narrower and mostly fall among the experimental pressure traces that are higher than the average. The LES calculation over-estimates the AHRR during the early combustion, which is similar to the LES result from the with-TP case. This results in a short ST-CA10 duration. Consequently, the simulation continues to predict a shorter CA10-90 with advanced CA50 timing, so both mean nIMEP and PCP magnitude are over-predicted. In Fig. 13(c), as Matekunas discussed in [43], the experimental data exhibits the hook-back of the curve and asymptotically reaches the slow burn as the PCP magnitude lowers and the PCP timing advances. This behavior is also not captured in the LES result. The fast growth of the flame kernel (*i.e.*, short ST-CA10) reduces the possibility of slow-burn, so the predicted COV_{nIMEP} and COV_{PCP} are largely off from the experimental data. Overall, the current LES is not capable of reproducing the combustion characteristics of the dilute combustion when the intensities of tumble and turbulent flows decrease. Further investigation is needed to identify which modeling approaches (grid size, turbulence model, and combustion model) cause the prediction failure, especially during the main combustion process (CA10-90). Also, as aforementioned, an advanced ignition model is needed to obtain the CA10 timing accurately.

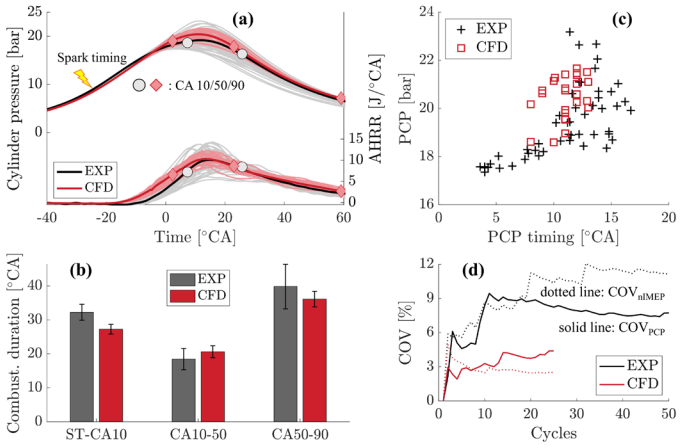

© 2022 by ASME

FIGURE 13: Comparison of experimental data and LES result from w/o TP case for (a) cylinder pressure and AHRR; (b) combustion duration; (c) correlation between PCP timing and magnitude; (d) convergence histories for COV_{PCP} and COV_{nIMEP} over the cycles.

TABLE 7: Key combustion metrics of w/o TP case.

		EXP	LES	Error [%]
Combustion duration [°CA]	ST-CA10	32.2	27.3	-15.2
	CA10-50	18.4	20.6	12.0
	CA50-90	39.8	36.1	-9.3
nIMEP [bar]		2.97	3.40	14.5
COV_{nIMEP} [%]		11.1	2.5	-8.6 (abs.)
PCP [bar]		19.4	20.5	5.7
COV_{PCP} [%]		7.6	4.3	-3.3 (abs.)

5. CONCLUSION

Enabling simulation-based optimization of engine geometry and operating strategy requires accurate prediction of the spray, mixing, and combustion processes. This study compares current standard approach with state-of-the-art models developed in the PACE program, in their LES predictions for a DISI engine with and without a tumble plate. Two sets of 25 LES cycles (one with and one without the tumble plate) are compared with the experimental data obtained from the optical engine, and the major conclusions from the results and discussion are as follows:

- By adopting the PACE best-practices for flash-boiling spray, the spray-collapse behavior under the flash-boiling condition is properly reproduced, whereas the standard flash-boiling model only accounting for phase-change, does not predict any deflected spray plumes.
- Both the Corrected Distortion model and SWI model accurately estimate the droplet drag and spray wall-impingement, leading to realistic liquid spray structure and spray footprint during the spray processes.
- The flame kernel initialization occurs at the spark timing with the standard ignition model, leading to an earlier heat release rate rise and shorter ST-CA10 duration in the LES result, compared to the experiments. The discrepancy becomes larger when the tumble plate is removed.
- The LES result reasonably reproduces the CCV in the case with tumble plate. The combustion rate is primarily correlated with the turbulent kinetic energy, while the flow distribution also significantly impacts the flame propagation. On the contrary, the CCV in the case without tumble plate is not captured and is significantly underestimated compared to the experimental data.

To improve the simulation accuracy, advanced ignition models that account for the evolution of the spark channel (elongation, short-circuit, blow-out/restrike) and for the growth of early flame kernel under dilute mixture conditions are needed. Also, further investigation is needed for the current modeling approaches in the grid size, turbulent flow, and combustion to better reproduce the combustion characteristics with respect to the design changes.

ACKNOWLEDGEMENTS

The submitted paper has been created by UChicago Argonne, LLC, operator of Argonne National Laboratory ("Argonne"). Argonne, a U.S. Department of Energy (DOE) Office of Science laboratory, is operated under Contract No. DE-AC02-06CH11357. The U.S. Government retains for itself, and others acting on its behalf, a paid-up nonexclusive, irrevocable worldwide license in said article to reproduce, prepare derivative works, distributed copies to the public, and perform publicly and display publicly, by or on behalf of the Government. Part of this work was performed at the Combustion Research Facility, Sandia National Laboratories, Livermore, CA. Sandia National Laboratories is a multi-mission laboratory managed and operated by National Technology and Engineering Solutions of Sandia, LLC., a wholly-owned subsidiary of Honeywell International, Inc., for the U.S. DOE's National Nuclear Security Administration under Contract No. DE-NA0003525. This paper describes objective technical results and analysis. Any subjective views or opinions that might be expressed in the paper do not necessarily represent the views of the U.S. Department of Energy or the United States Government.

This research was conducted as part of the Partnership to Advance Combustion Engines (PACE) sponsored by the U.S. DOE Vehicle Technologies Office (VTO). A special thanks to DOE VTO program managers, Mike Weismiller and Gurpreet Singh. In addition, the authors gratefully acknowledge the computing resources provided on Bebop, a high-performance computing cluster operated by the Laboratory Computing Resource Center at Argonne National Laboratory.

REFERENCES

[1] "Inventory of U.S. Greenhouse Gas Emissions and Sinks: 1990-2020," EPA, 2022. Available (access date: 4/28/2022): https://www.epa.gov/ghgemissions/inventory-us-greenhouse-gas-emissions-and-sinks-1990-2020.

[2] "The Safer Affordable Fuel-Efficient (SAFE) Vehicles Rule for Model Years 2021–2026 Passenger Cars and Light Trucks." EPA and NHTSA, pp. 24174–25278, 2020.

[3] K. Nakata, S. Nogawa, D. Takahashi, Y. Yoshihara, A. Kumagai, and T. Suzuki, "Engine Technologies for Achieving 45% Thermal Efficiency of S.I. Engine," SAE Int. J. Engines, Vol. 9 No. 1 (2015): pp. 179–192. doi: 10.4271/2015-01-1896.

[4] S. Matsuo, E. Ikeda, Y. Ito, and H. Nishiura, "The New Toyota Inline 4 Cylinder 1.8L ESTEC 2ZR-FXE Gasoline Engine for Hybrid Car," SAE Tech. Paper 2016-01-0684, 2016. doi: 10.4271/2016-01-0684.

[5] B. Lee, H. Oh, S. Han, S. Woo, and J. Son, "Development of High Efficiency Gasoline Engine with Thermal Efficiency over 42%," SAE Tech. Paper 2017-01-2229, 2017. doi: 10.4271/2017-01-2229.

 © 2022 by ASME

[6] N. Yoshida, “Development of New I4 2.5L Gasoline Direct Injection Engine,” SAE Tech. Paper 2019-01-1199, 2019. doi: 10.4271/2019-01-1199.
[7] Y. Yoshihara, K. Nakata, D. Takahashi, T. Omura, and A. Ota, “Development of High Tumble Intake-Port for High Thermal Efficiency Engines,” SAE Tech. Paper 2016-01-0692, 2016. doi: 10.4271/2016-01-0692.
[8] N. Hayashi, A. Sugiura, Y. Abe, and K. Suzuki, “Development of Ignition Technology for Dilute Combustion Engines,” SAE Int. J. Engines, Vol. 10 No. 3 (2017): pp. 2017-01–0676. doi: 10.4271/2017-01-0676.
[9] R. N. Dahms and J. C. Oefelein, “The significance of drop non-sphericity in sprays,” Int. J. Multiph. Flow, Vol. 86 (2016): pp. 67–85. doi: 10.1016/j.ijmultiphaseflow.2016.07.010.
[10] T. M. Nguyen, R. N. Dahms, L. M. Pickett, and F. Tagliante, “The Corrected Distortion model for Lagrangian spray simulation of transcritical fuel injection,” Int. J. Multiph. Flow, Vol. 148 (2022): 103927. doi: 10.1016/j.ijmultiphaseflow.2021.103927.
[11] H. Guo, R. Torelli, S. Som, N. Kim, D. L. Reuss, and M. Sjöberg, “In-cylinder sprays in a direct-injection spark-ignition optical engine. Part I: Effect of flash-boiling and intake crossflow on free-spray evolution,” (under preparation).
[12] R. Torelli et al., “Toward predictive and computationally affordable Lagrangian–Eulerian modeling of spray–wall interaction,” Int. J. Engine Res., Vol. 21 No. 2 (2020): pp. 263–280. doi: 10.1177/1468087419870619.
[13] R. Torelli, N. Kim, M. Sjöberg, and S. Som, “Large eddy simulations of spray-wall interaction in a direct-injection optical engine,” Large-Eddy Simulation for Energy Conversion in electric and combustion Engines (LES4ECE), Jun. 17-18, 2022.
[14] S. W. Wagnon, “Development of an Optimized Gasoline Surrogate Formulation for PACE Experiments and Simulations,” 2021. Available (access date: 4/28/2022): https://www.energy.gov/sites/default/files/2021-07/VTO_2020_APR_ADV_FUEL_COMPILED_REPORT_JUL_7_2021_compliant_.pdf.
[15] S. Cheng et al., “Autoignition and preliminary heat release of gasoline surrogates and their blends with ethanol at engine-relevant conditions: Experiments and comprehensive kinetic modeling,” Combust. Flame, Vol. 228 (2021): pp. 57–77. doi: 10.1016/j.combustflame.2021.01.033.
[16] M. J. McNenly, R. A. Whitesides, and D. L. Flowers, “Faster solvers for large kinetic mechanisms using adaptive preconditioners,” Proc. Combust. Inst., Vol. 35 No. 1 (2015): pp. 581–587. doi: 10.1016/j.proci.2014.05.113.
[17] S. Lapointe, R. A. Whitesides, and M. J. McNenly, “Sparse, iterative simulation methods for one-dimensional laminar flames,” Combust. Flame, Vol. 204 (2019): pp. 23–32. doi: 10.1016/j.combustflame.2019.02.030.
[18] D. L. Reuss, N. Kim, and M. Sjöberg, “The influence of intake flow and coolant temperature on gasoline spray morphology during early-injection DISI operation,” Int. J. Engine Res., 2022 (accepted).
[19] N. Kim, D. Vuilleumier, and M. Sjoberg, “Effects of Injection Timing and Duration on Fuel-Spray Collapse and Wall-Wetting in a Stratified Charge SI Engine,” SAE Tech. Paper 2021-01-0544, 2021. doi: 10.4271/2021-01-0544.
[20] J. B. Heywood, “Internal Combustion Engine Fundamentals”, 1st Ed. McGraw-Hill, New York (1988).
[21] M. Sjöberg, D. Vuilleumier, N. Kim, N. Yokoo, T. Tomoda, and K. Nakata, “On the Role of Nitric Oxide for the Knock-Mitigation Effectiveness of EGR in a DISI Engine Operated with Various Gasoline Fuels,” SAE Int. J. Adv. Curr. Pract. Mobil., Vol. 2 No. 1 (2019): pp. 272–291. doi: 10.4271/2019-01-2150.
[22] Convergent Science Inc., “CONVERGE 3.0 Manual.” Madison, WI, 2020.
[23] T. Poinsot, “Requirements and validations for LES tools in combustion,” Large-Eddy Simulation for Internal Combustion Engine (LES4ICE), 2016.
[24] C. Xu, S. Som, and M. Sjöberg, “Large Eddy Simulation of Lean Mixed-Mode Combustion Assisted by Partial Fuel Stratification in a Spark-Ignition Engine,” J. Energy Resour. Technol., Vol. 143 No. 7 (2021). doi: 10.1115/1.4050588.
[25] E. Pomraning, “Development of Large Eddy Simulation Turbulence Models,” Ph.D. Thesis, University of Wisconsin-Madison, Madison, WI, 2000.
[26] R. D. Reitz and R. Diwakar, “Structure of high-pressure fuel sprays,” SAE Tech. Paper 870598, 1987. doi: 10.4271/870598.
[27] J. C. Beale and R. D. Reitz, “Modeling Spray Atomization with The Kelvin-Helmholtz/Rayleigh-Taylor Hybrid Model,” At. Sprays, Vol. 9 No. 6 (1999): pp. 623–650. doi: 10.1615/AtomizSpr.v9.i6.40.
[28] A. A. Amsden, P. J. O’Rourke, and T. D. Butler, “KIVA-II: A computer program for chemically reactive flows with sprays,” Los Alamos, NM, 1989. doi: 10.2172/6228444.
[29] N. Peters, “Turbulent Combustion.” Cambridge University Press, Cambridge (2000).
[30] Z.-G. Feng and E. E. Michaelides, “Drag Coefficients of Viscous Spheres at Intermediate and High Reynolds Numbers,” J. Fluids Eng., Vol. 123 No. 4 (2001): pp. 841–849. doi: 10.1115/1.1412458.
[31] Z.-G. Feng and E. E. Michaelides, “Heat and mass transfer coefficients of viscous spheres,” Int. J. Heat Mass Transf., Vol. 44 No. 23 (2001): pp. 4445–4454. doi: 10.1016/S0017-9310(01)00090-4.
[32] A. Richter and P. A. Nikrityuk, “Drag forces and heat transfer coefficients for spherical, cuboidal and ellipsoidal particles in cross flow at sub-critical Reynolds numbers,” Int. J. Heat Mass Transf., Vol. 55 No. 4 (2012): pp. 1343–1354. doi: 10.1016/j.ijheatmasstransfer.2011.09.005.
[33] P. J. O’Rourke and A. A. Amsden, “The Tab Method for Numerical Calculation of Spray Droplet Breakup,” SAE Technical Paper 872089, 1987. doi: 10.4271/872089.
[34] G. M. Faeth, “Current status of droplet and liquid combustion,” Prog. Energy Combust. Sci., Vol. 3 No. 4, (1977): pp. 191–224. doi: 10.1016/0360-1285(77)90012-0.

 © 2022 by ASME

[35] S. E. Parrish and R. J. Zink, “Spray characteristics of multi-hole injectors under flash boiling conditions,” 21st ILASS Americas, May 18-21, 2008.
[36] J. Senda, Y. Hojyo, and H. Fujimoto, “Modelling of Atomization Process in Flash Boiling Spray,” SAE Tech. Paper 941925, 1994. doi: 10.4271/941925.
[37] M. Adachi, V. G. McDonell, D. Tanaka, J. Senda, and H. Fujimoto, “Characterization of Fuel Vapor Concentration Inside a Flash Boiling Spray,” SAE Tech. Paper 970871, 1997, doi: 10.4271/970871.
[38] Y. Zeng and C.-F. F. Lee, “An Atomization Model for Flash Boiling Sprays,” Combust. Sci. Technol., Vol. 169 No. 1 (2001): pp. 45–67. doi: 10.1080/00102200108907839.
[39] H. Pitsch, “A G-equation formulation for large-eddy simulation of premixed turbulent combustion,” Annual Research Briefs, 2002, p. 12.
[40] P. J. O’Rourke and A. A. Amsden, “A Spray/Wall Interaction Submodel for the KIVA-3 Wall Film Model,” SAE Tech. Paper 2000-01-0271, 2000. doi: 10.4271/2000-01-0271.
[41] S. J. Kazmouz et al., “High-Fidelity Energy Deposition Ignition Model Coupled with Flame Propagation Models at Engine-Like Flow Conditions,” Proc. ASME 2021 Int. Combust. Engine Division Fall Tech. Conference. Oct. 13-15, 2021, doi: 10.1115/ICEF2021-67598.
[42] S. J. Kazmouz et al., “Coupling a Lagrangian-Eulerian Spark-Ignition Model with LES Combustion Models for Engine Simulations,” Sci. Technol. Ener. Trans., 2022 (accepted).
[43] F. A. Matekunas, “Modes and Measures of Cyclic Combustion Variability,” SAE Tech. Paper 830337, 1983. doi: 10.4271/830337.

© 2022 by ASME